Anisotropic deformation and failure behaviors of the necked HDPE materials induced by oligo-cyclic loading

Hang Guo, R.G. Rinaldi, Morgane Broudin, Sourour Tayakout, Olivier Lame

Version of Record: https://www.sciencedirect.com/science/article/pii/S0032386121008557
Manuscript_8e289d618cc997ec3e77d8785d01258e

Anisotropic deformation and failure behaviors of the necked HDPE materials induced by oligo-cyclic loading

Hang GUO[1], Renaud G. RINALDI[1], Morgane BROUDIN[2], Sourour TAYAKOUT[3], Olivier LAME[1]*

[1)] Université de Lyon, CNRS, INSA-Lyon, MATEIS, UMR5510, 69621, Villeurbanne, France

[2)] EDF-R&D Lab Les Renardières, Avenue des Renardières-Ecuelles, F-77250, Moret-Loing-et-Orvanne, France

[3)] EDF-DIPNN-Direction Technique, 19 rue Pierre Bourdeix, F-69007, LYON, France

*Corresponding authors: Olivier LAME

E-mail: olivier.lame@insa-lyon.fr

ABSTRACT

Oligo-cyclic loading tests are performed between a fixed nominal macroscopic strain 1.5 and zero force on high-density polyethylene (HDPE) with different microstructural properties (i.e. crystallinity, lamellar dimensions, density of stress transmitters). Based on the results of simultaneous Digital Image Correlation (DIC), the local strain is significantly localized when the macroscopic strain exceeds the elastic limit, confirming the necking propagation during the first loading path. Upon the consecutive cycles, the accumulation of longitudinal residual strain (along tensile direction) mainly occurs in the necked region, whereas the transverse reduction remains limited. The anisotropic deformation and failure behaviors of the necked region is systematically investigated using combined tensile tests and synchrotron small angle X-ray scattering. Along the longitudinal direction, the deformation of the necked sample is mainly ascribed to the inter-fibrillar region, where the chains can be deformed more easily than the ones located in the intra-fibrillar region. Along the transversal direction, a clear reorientation of the microfibrils can be observed and interpreted as the rotation of crystal blocks. Due to the similar microstructural parameters of lamellar stacks in the two directions, the anisotropic failure behaviors of the pre-loaded sample may be induced by the different density of chain between the intra- and inter- fibrillar regions or the easier growth of the oriented cavities due to the transversal stretching.

KEYWORDS: High-Density Polyethylene, Digital Image Correlation, necking, oligo-cyclic loading, fibrillar structure, *in-situ* Small Angel X-ray Scattering

INTRODUCTION

The use of High-Density Polyethylene (HDPE) as the constitutive material to design pipelines is now widely spread. One of their advantages compared to conventional metal-based pipes is their convincing capability to resist the impact, high-cycle fatigue, and seism-like damage. For instance, in 2018, according to the report of Polyethylene Piping System Integrated Technology ＆Engineering Center in Japan, HDPE pipelines remained almost undamaged after the seismic activity[1]. In order to model a seismic event, oligo-cyclic testing conditions involving plastic deformation and a limited amount of loading cycles[2–4] are often used. It is similar to the low cycle fatigue test[5–7]. Under a real seism-like condition, the loading mode for a certain pipeline in a global architecture can be complex (combination of the tension, bending, compression and so on) due to the complicated connection between each other[4]. In the literatures, efforts are mainly paid to understand the seism-like (low-cycle fatigue) performance of the whole architecture (e.g. piping system[8]) rather than the associated macro-micro correlation under oligo-cyclic loading conditions. Damage is often described by the deterioration of mechanical properties (such as stiffness, failure stress) or fracture mechanics such as J-integral and essential work of fracture [9–15]. To simplify the study of macro-micro correlation, we here focus on the uniaxial tensile deformation.

When HDPE and/or other semi-crystalline polymers are submitted to plastic deformation, they potentially exhibit various macroscopic phenomena, such as necking[16–21], whitening (cavitation)[22–28] and buckling[20], etc. In particular, under uniaxial tensile elongation, necking is recognized as the manifestation of plastic instability[17,18,29,30] and a failure mode[20]. The necking (strain localization) is initiated due to pre-existing “weak points”, such as a structural defect or a geometrical artifact for instance. When the strain along tensile direction locally reaches a critical value, designated as natural draw ratio, λ_n, the growth of local strain is somehow completed and similar mechanisms then occur in the nearby regions[17,30], so the neck finally propagates throughout the entire gauge length of the tensile specimen. Occurring

within a sample of constant cross-section, the propagation phase is seen to develop at quasi-constant force. Also, as the neck propagates, the local strain within the necked region may also slightly increase due to the potential plastic creep[31,32]. At the end of propagation, the axial strain is almost spatially homogenous within the entire gauge length of the sample. As for the macroscopic evaluation and characterization of necking behavior, the neck width and natural draw ratio obtained from nominal stress-strain profiles are often recognized as the relevant indicators[18,33]. Moreover, infrared imaging[34], local strain measurement by Electronic Speckle Pattern Interferometry (ESPI)[35], and full-field displacement measurement by Digital Image Correlation (DIC) technique[16,19,36,37] have also been applied. Among these techniques, DIC measurement deserves particular attention due to its high accuracy and immediacy. This technique allows for tracking of the displacement field of a speckled pattern (subdivided into subsets) added onto the surface of a sample. Real-time image recording of the specimen is performed, and a subsequent image analysis leads to the determination of the surface or volumetric[38] (for the case of the sample with cylindrical cross-section) strain fields.

At the microscopic scale, the necking behavior depends on the density of stress transmitters (STs) as ties, entanglements and loops that link the crystalline/amorphous phases. These elements operate at the scale of lamellar stacks (nanoscale). PE with lower ST density tend to exhibit higher plastic deformation heterogeneity[18,39]. Whatever the pristine microstructures, within the already-necked region, the original isotropic spherulites in PE material are transformed into highly oriented microfibrils composed of fragmented/oriented crystalline blocks connected by stretched STs in the amorphous phase. These fibrils play an important role in preventing the crack/craze propagation[24,40–42]. The *so-called* fibrillar transformation[43–46] is physically interpreted as destruction-recrystallization or melting/recrystallization mechanisms[43–45,47].

Janssen et al.[48,49] mentioned that necking is a major mode of fatigue failures (ductile type) in the oligo-cyclic regime (or thermally-dominated domain), differing from the brittle failure as cracking in the high-cycle regime (or mechanically-dominated domain). Some authors have also drawn the similar conclusion in their works[20,50]. The necking may be also accompanied by cavitation, which induces the volumetric strain and strongly affected by the microstructure of semi-crystalline polymers [22–24,51], temperature [22,51], and stress triaxiality[28]. Experimentally, the cavitation can be quantitatively characterized by densitometry [41],

volumetric strain measurements [25], SAXS [22,25,51,52], and positron annihilation lifetime spectroscopy (PALS) [53] etc. Among them, the increase of the sample's volume upon uniaxial stretching is generally considered as the most direct physical evidence of the cavity formation. Therefore, it is worth investigating the necking/strain heterogeneities taking place under the oligo-cyclic loading conditions with the objective to improve the understanding of the oligo-cyclic performance of HDPE. In addition, the material within the necked region being in an "extreme" deformed state, the characterizations of its further mechanical properties and associated deformation behaviors are important for the qualification of the pre-loaded HDPE pipelines by the earthquake or low cycle fatigue. The comparison of the failure properties between the pristine and pre-loaded samples can contribute to the damage evaluation and the deformation mechanisms are helpful to understand its origin. Also, due to the cyclic-loading induced orientation of the microstructure, the anisotropy evaluation should also be of great interest[16,53].

EXPERIMENTAL SECTION

Shaping process and microstructure characterizations

Two groups of commercial HDPE pellets were ordered from INEOS (Brussels, Belgium), and denoted as PE-A and PE-B, they are used for blow-molding and pipeline application (PE-100) respectively. Some basic information about the pellets are listed in **Table 1S** of the supporting information, including the primary molecular parameters, peak value of crystallization temperature (T_c), melting temperature (T_m), onset of degradation temperature (T_d) and weight fraction of additives (Ad.). Due to the difference in molecular properties, the two PE grades show different sensibility of crystallization to the thermal treatments, and different ability to create stress transmitters during the crystallization. It means that after the similar crystallization history, their microstructural properties (crystallinity, lamellar dimensions, ST density, etc.) are significantly different. Consequently, by changing the crystallization conditions, the HDPE samples with a large range of crystallinity/density of stress transmitters can be generated. The pellets were firstly compression-molded into 0.8 mm thick sheets. Different thermal treatments (quenching in cold water and isothermal treatment in the oil bath at a selected temperature in the vicinity of the crystallizing one, the detail for the selection has been presented in our anterior work[54]) were then imposed in order to generate the samples with a range of microstructural

properties (e.g. varying crystallinity and density of stress transmitters) thanks to the different regimes of crystallization [55]. Once shaped, the pristine microstructures were characterized: the crystallinity was measured by Differential Scanning Calorimetry (DSC) technique, the long period and thickness of lamellar stacks were characterized by SAXS, the ST density was estimated by both tensile characterization (neck width[18,33]) and Brown's model[56–58] (see our previous work for further details[33]).

The results are summarized in the following **Table 1.** The four samples under consideration show a range of crystallinity varying from 57% to 73%. Relatively lower value of ST density is observed in the samples having higher crystallinity. All in all, under identical processing condition, the PE-B material has lower crystallinity and more ST elements than the PE-A. For a given grade, isothermal sample has higher crystallinity but lower ST concentration. This result is in accordance with the previous observation in the literature[18].

Table 1. Microstructure characteristics of HDPE after shaping process.

Methods		DSC	SAXS			Brown's model	Neck width
Microstructure characteristics		X_c (%)	L_p (nm)	L_c (nm)	L_a (nm)	[ST]	
PE-A	Quenched	62(±1)	22	13	9	0.22	0.55(±0.05)
	Isothermal	73(±1)	35	24	11	0.07	0.27(±0.05)
PE-B	Quenched	57(±1)	20	11	9	0.27	0.65(±0.05)
	Isothermal	64(±1)	33	20	13	0.14	0.32(±0.05)

Mixed-mode oligo-cyclic tests with simultaneous Digital Image Correlation (DIC)

Dumbbell-shaped specimens of 14 mm gauge length, 12 mm width, and 0.8 mm thickness were punched from the shaped sheets. Spray paint was used for preparing the speckled pattern in the zone of interest (14×12 mm^2) in DIC analysis. At least 15min separated the painting from the test to leave sufficient time for the paint to dry. The specimens were subjected to 10 repeated

loading-unloading cycles at a constant nominal strain rate $\dot{\varepsilon}=1\times10^{-2}s^{-1}$ using an MTS 1/ME machine with a 5KN load cell. For each test, the specimens were stretched up to a selected macroscopic strain $\varepsilon_{OC}=1.5$ and unloaded till reaching the zero-stress state. When $\varepsilon_{OC}=1.5$, the necked region should be already initiated in each sample according to the stress-strain relation (see **Figure 1S** in the supporting information). Simultaneously, CCD camera was installed to capture the sample images, the time interval between two images is 0.5s. The commercial software *VIC-3D* from *correlated solutions*® was employed to perform the correlation process and strain mapping generation in the painted surface. The accuracy of the local strain is 0.01.

With this imposed strain ε_{OC}, the local strain mapping for the entire gauge length can be completely correlated and recorded during the tests. Moreover, for each sample, the necked region is long and large enough for punching the mini samples for post tensile tests, which will be mentioned in the next section. After the tests, all pre-loaded specimens were stored at room temperature for about 1 month, to ensure sufficient relaxation before the following tests.

Post tensile tests with/without in-situ SAXS characterizations

To compare the deformation behaviors at both macro- and micro- scales of the pristine and necked materials, three specimens were prepared for each material listed in **Table 1:** 1) a "Pristine" sample was directly punched from the sheet, 2) a "L-necked" sample was cut out along the longitudinal (pre-stretching) direction in the necked region of the sample that beforehand experienced oligo-cyclic loading, 3) Following the same procedure, the "T-necked" specimen was cut perpendicular to the tensile loading direction of another pre-conditioned sample. A small dumbbell-shaped cutter with a gauge length of 3.5 mm in length and 2 mm in width was used for the sample preparation.

(1) With in-situ SAXS characterizations

Uniaxial loading tests up to failure were performed with a homemade uniaxial testing machine at room temperature (about 25°C). The nominal strain rate was 3×10^{-3} s^{-1}. *In-situ* SAXS characterizations were carried out on the SWING beamline at the SOLEIL synchrotron in France. The wavelength of the X-ray was 1.03 Å and the specimen-detector distance was 2003 mm so that the scattering information could be observed in a 2D q-window with the range 0.036-0.52 $Å^{-1}$. The time interval between two consecutive SAXS acquisitions is 3s and the exposure

time is 0.5s. With this strain rate and testing conditions of SAXS, the time resolved microstructure evolution can be precisely recorded.

(2) Without in-situ SAXS characterizations

Moreover, to consolidate the investigation of the pre- and post- oligo-cyclic loading end-of-life (failure) properties, especially the failure stress, additional tensile characterizations were performed using an MTS 1/ME machine equipped with a 100N load cell. The testing conditions were replicated and each test was repeated at least three times, with the average values and standard deviations being recorded. **Figure 1** illustrates the mechanical and *in-situ* SAXS testing procedure**.**

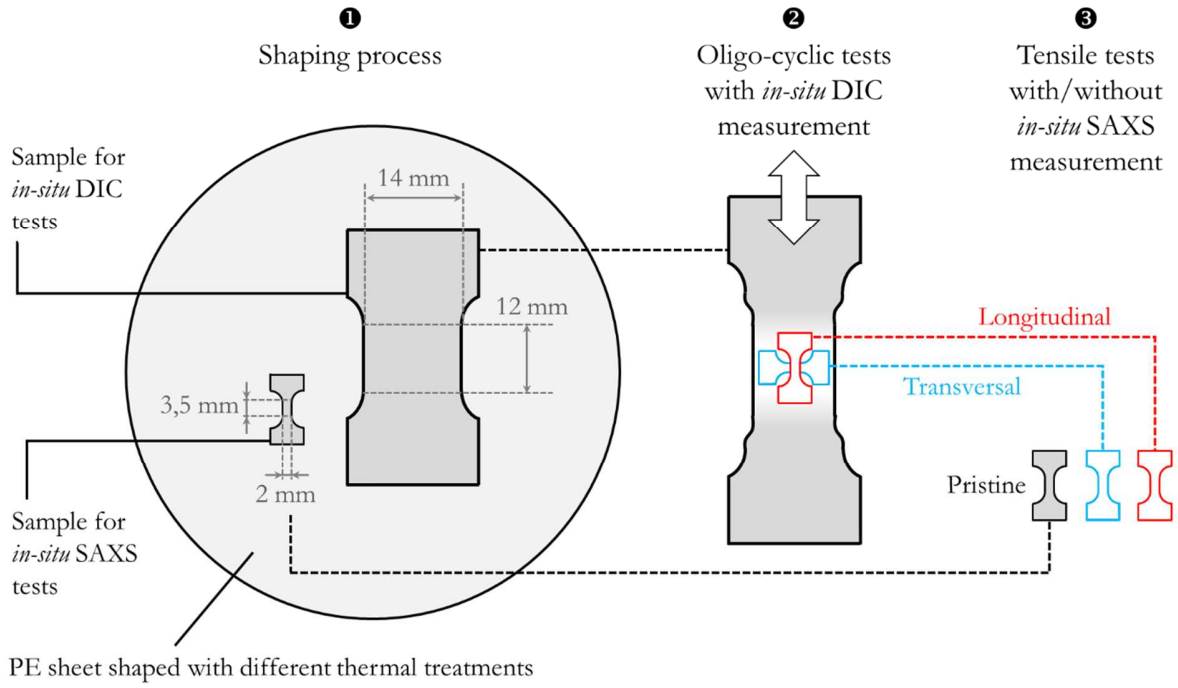

Figure 1: Overview of the mechanical and *in-situ* SAXS testing procedure.

RESULTS AND DISCUSSION

Strain localization and accumulation

The strain localization is evaluated by DIC analysis. For instance, **Figure 2a** plots the evolution of the macroscopic nominal strain with respect to the time in PE-A quenched material during the mixed-mode cyclic test. The residual strain at zero stress evolves as the cycle number increases

during a test (see the values reported in **Figure 2a** for the 1st and 10th unloaded states). The spatial distribution of the X-oriented (longitudinal, i.e. parallel to the loading direction) and Y-oriented (transversal) nominal strain components can be recorded along with the time/macroscopic strain evolution. As an example, **Figure 2b and c** illustrate the longitudinal and transverse strain mappings at the end of the first loading process (in the maximum-strain state), clearly, the strain components are heterogeneous and a clear necked region is observed.

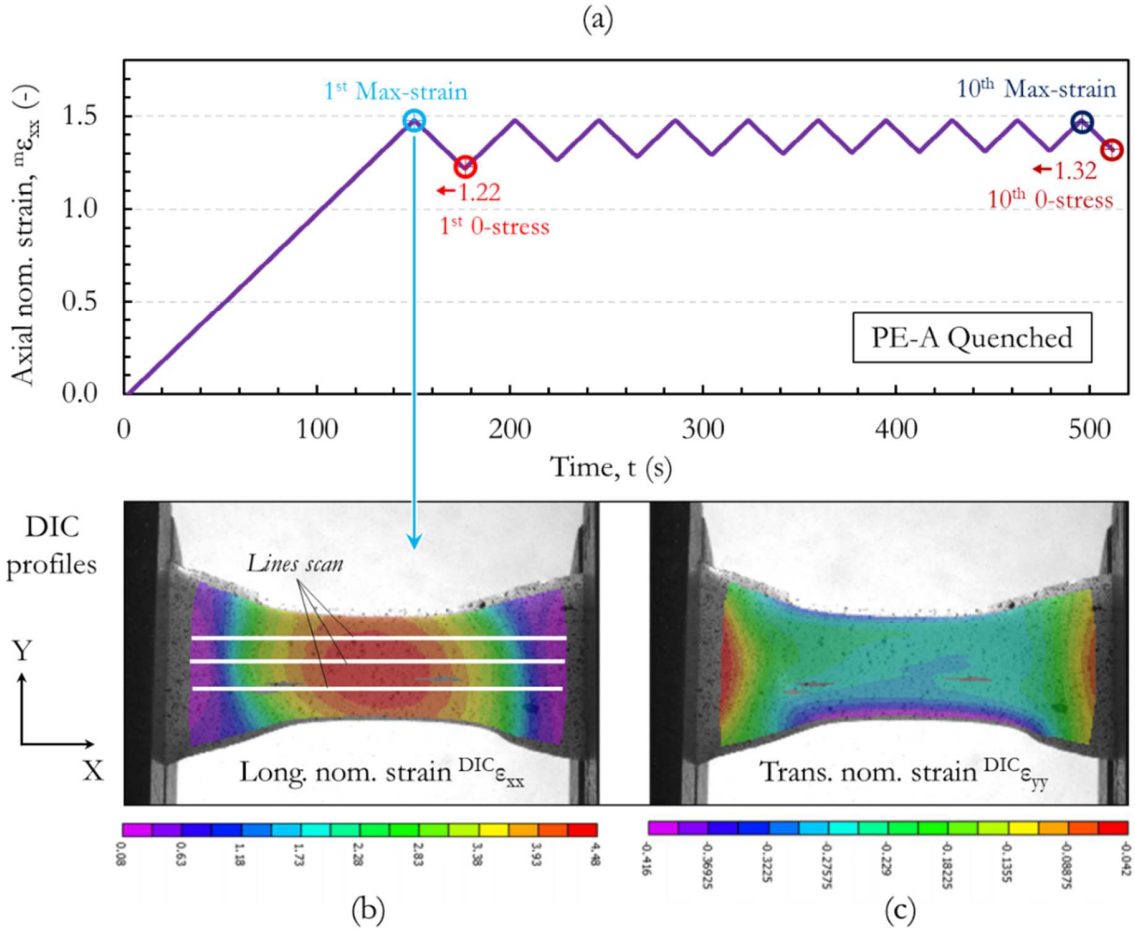

Figure 2: Oligo-cyclic tensile loading with in-situ DIC measurement of PE-A quenched sample: (a) macroscopic strain-time profile prescribed by the testing machine; (b) longitudinal strain mapping at the end of the first loading; (c) transversal strain mapping at the end of the first loading.

Further quantitative data reductions are pursued: to simplify and highlight the evolution of strain localization with increasing cycles, the potential through-width variations are omitted and the longitudinal and transverse strain components are now determined as a function of the X-position. The values obtained from three line-scans are displayed in **Figure 2b:** each line is

discretized into 200 elements and the local strains for a given X-position is determined by averaging the values collected by the three lines. The X- and Y-oriented strain profiles with respect to the X-position are presented in **Figure 3**.

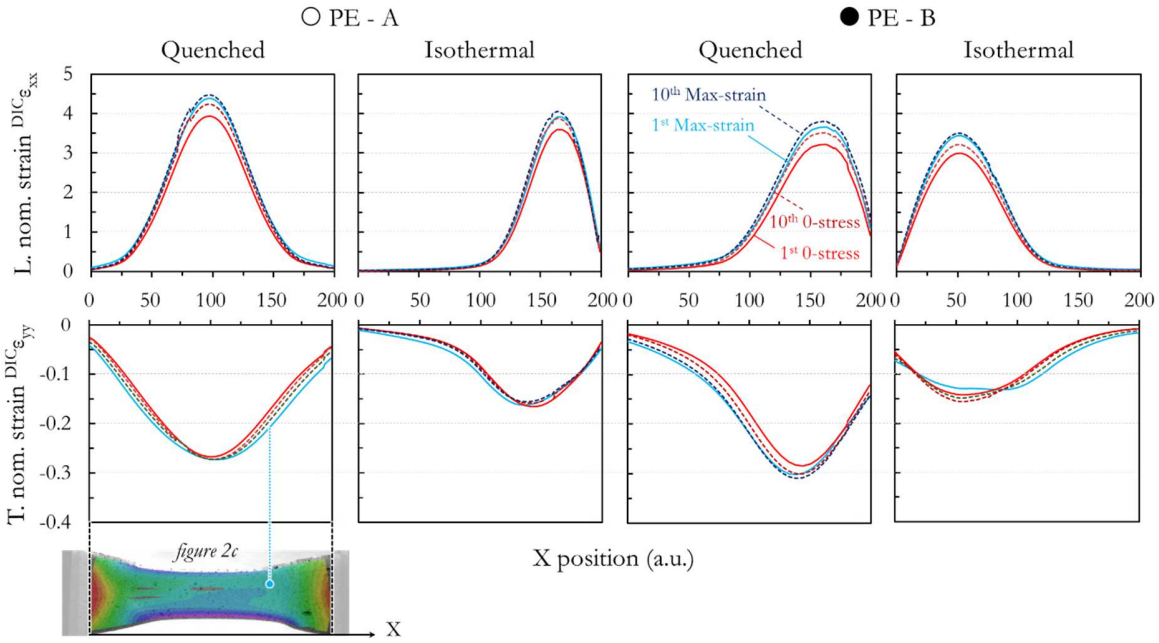

Figure 3: Longitudinal (L.) and transversal (T.) nominal strain distributions as a function of X-position at 4 stages during the oligo-cyclic test (N.B. the bottom left image recalls the transverse nominal strain field at the end of the first loading step).

Data for all four materials in the maximum-strain and zero-stress states of the 1st and 10th cycles are plotted. Considering the aforementioned remarks regarding the neck initiation and its sensitivity to "weak points", it is not surprising that the X-position of the maximum local strain differs within these samples. Focusing on the first maximum-strain state, the maximum local longitudinal strains range between 3.5 and 4.5 in all samples (i.e. taking the smaller value as the reference, the relative difference is within 15% in different samples), yet being much higher than the prescribed macroscopic one (1.5). Along the transversal direction, the local strain value shows a great dependency on thermal treatment: the quenched samples exhibit a remarkable reduction of width in the necked region (local strains are about -0.3), whereas the peak values of the transverse strain in isothermal samples are only about -0.2. The relative difference is thus about 50%.

In the zero-stress state, by comparing the local strain profiles between the 1st and the 10th cycles, it can be observed that the longitudinal strain accumulation is still localized in the necked region. However, along the transverse direction, limited accumulation effect can be observed.

Beyond the elastic limit, a semi-crystalline material is supposed to undergo isochoric deformation when voids generation does not occur. Therefore, a volumetric strain differing from 0, yet positive can be attributed to the voids/cavitation[23,25]. The dimension evolution along the z-axis (direction of thickness) could not be measured in real-time with the experimental setup available. However, by comparing the sample thicknesses in the undeformed and the 10th zero-stress state with a caliper (three measurements were averaged within the region with highest axial local strain), the corresponding local strain can be approximately evaluated. The contraction (strain) along z-axis ε_{zz} (about -0.7 in every sample) is significantly different from that along the y-axis, ε_{yy}. This anisotropy may be attributed to the gradient of microstructure induced skin-core effect [59] or deformation gradient through the thickness despite homogenous microstructure in the necked region[60]. The volumetric strain can be thus estimated using **equation (1)** below:

$$\frac{\Delta V}{V_0} = (1 + \varepsilon_{xx})(1 + \varepsilon_{yy})(1 + \varepsilon_{zz}) - 1 \quad (1)$$

To estimate the maximum local volumetric strain, the peak values of ε_{xx} and ε_{yy} are taken into account for this calculation. The results of the four materials are presented in **Figure 4** as a function of the crystallinity and a good correlation is observed between the maximum local volumetric strain and the microstructure of the samples.

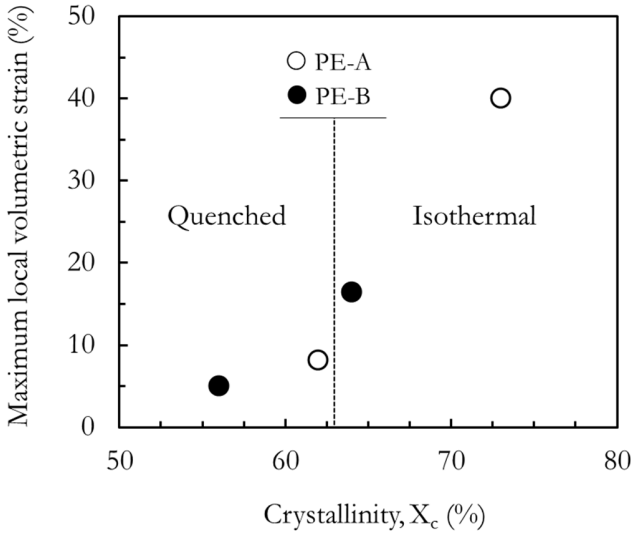

Figure 4: Maximum local volumetric strain at the final zero-stress state as a function of sample crystallinity.

More precisely, the isothermal samples with higher crystallinity and lower ST density show a stronger volumetric variation after the same loading history, in particular, the PE-A one. Conversely, the two quenched samples show only slight volumetric variation (inferior to 10%). This dependency is in accordance with our previous results about the cavity volume fraction and dimensions obtained by *in-situ* SAXS characterizations[54].

Anisotropic deformation behavior in the necked HDPE materials

Qualitative descriptions at macroscale

Although the mechanical/deformation behaviors undoubtedly differ with respect to the thermal treatment (as shown in **Figure 5**) and material type, in the following, the qualitative descriptions and discussions are mainly focused on the differences among the pristine, L- and T-necked samples of the same grade to highlight the changes and anisotropy induced by the oligo-cyclic loading. Only the results of PE-B samples are presented due to the similar qualitative observations for the PE-A samples.

The nominal stress-strain responses of the Pristine, L- and T-necked samples submitted to uniaxial elongation up to macroscopic strain ε=1.5 are presented in **Figure 5a**. The nominal stress-strain curves up to failure for the four materials are provided in **Figure 2S** in the supporting information. The loading direction is horizontal. They strongly differ in terms of

nominal stress magnitude and profile. Different macroscopic deformation behaviors are also explored as the test proceeded by recording simultaneous 2D images of the samples using a CCD camera as illustrated in **Figure 5b and 5c** (PE-B samples). Four representative deformation states (ε=0, 0.15, 0.5, and 1) are presented for each sample. According to the results, the L-necked samples show limited necking and stress softening during elongation. However, both the pristine and T-necked samples present strain localization behaviors, especially the T-necked samples for which the width reduction is highly pronounced. Consequently, the nominal stress softening in T-necked samples is much more significant (the stress softening is about 45%-50%, taking the yield stress as the reference) than the pristine ones (20%-25%).

Due to the different strain localization (necking) levels until ε=1.5, the nominal stress values are not representative and comparable during this phase, the true stress should be considered instead. Taking into account the potential voids, especially for the pristine isothermal samples, the traditional isochoric assumption is not suitable for the true stress calculation. However, the failure stress can still be estimated in the vicinity of the failure/fracture point, where the section of specimen can be measured after the fracture in tensile test (the neck propagation is finished at this moment). The analysis of the failure stress will be further discussed in the next section combined with the micro-mechanism.

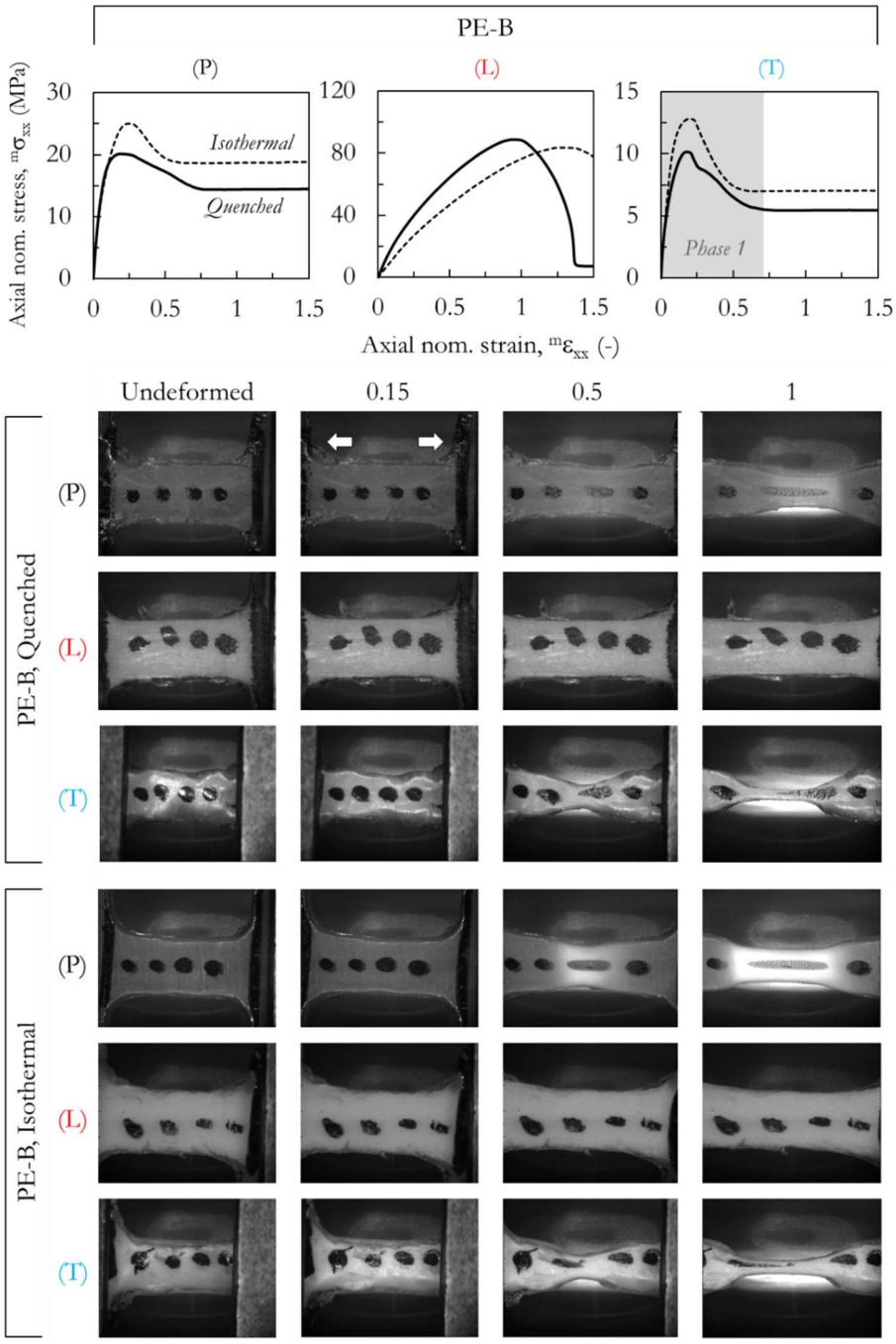

Figure 5: Tensile nom. stress - nom. strain profiles in the pristine (P), L-necked (L) and T-necked (T) samples of PE-B materials (on top). Companion pictures of the specimen for four stages (on bottom).

Quantitative analysis at microscale

At microscale, *in-situ* SAXS measurement allows coupling the macroscopic deformation behavior with the evolution of the material microstructure. The SAXS 2D patterns obtained for

the same four deformation stages as the 2D sample images are presented in **Figure 6**. Also, the stretching direction is horizontal (as marked in the second image of the first line).

Focusing on the pristine samples composed of the spherulites, they display the isotropic ring-shaped 2D SAXS patterns in the undeformed state, confirming the presence of randomly oriented lamellae in the isotropic spherulite, which are then progressively transformed to the *lobe-like* shapes indicating the fibrillar structure[43,44] with increasing macroscopic strain. The stronger scattering intensity in the center of the SAXS patterns suggests a pronounced cavitation phenomenon in the isothermal sample. It is in accordance with the macroscopic sample whitening observed in the necked region (see **Figure 5**). As for necked samples (L and T), the initial *lobe-like* patterns indicate that the microstructures of both quenched and isothermal samples have already transformed into the fibrillar structure during the oligo-cyclic pre-loading process. In the L-necked samples, the configuration of the SAXS pattern remains constant qualitatively, whereas, in the T-necked samples, a 90° re-orientation of the structures can be observed with increasing strain up to 1. The deformation behaviors of fibrillar structures in L- and T-necked samples can be quantitatively described based on the evolution of two microstructural dimensions: the long period and the average width of micro-fibrils.

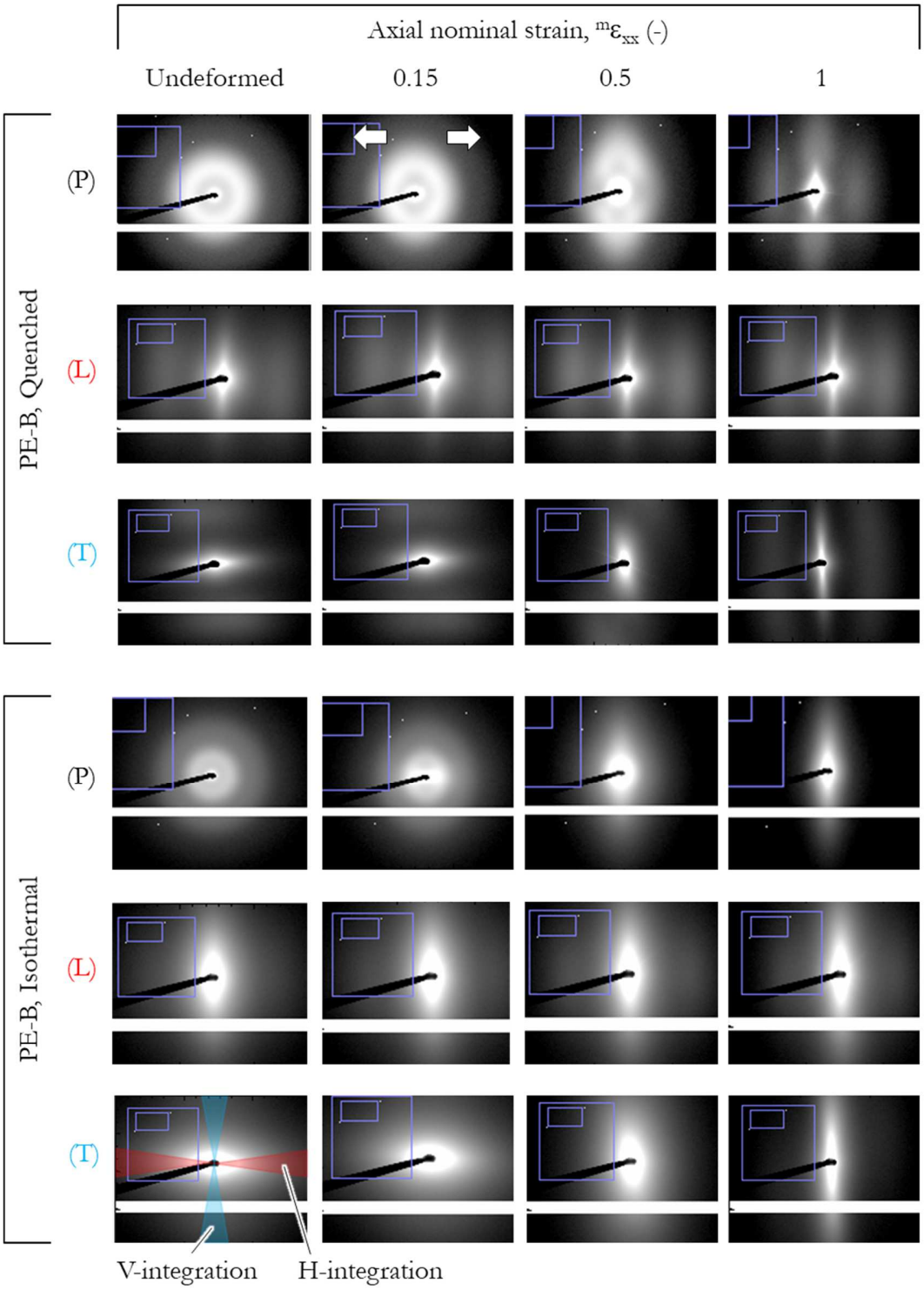

Figure 6: Evolution of the SAXS patterns along with the deformation in Pristine (P), L-necked (L) and T-necked (T) PE-B samples.

L-necked samples:

Firstly, the deformation behavior of the L-necked samples is analyzed, it is also compared with the behavior in pristine samples in the elastic regime.

For measuring local long periods, the azimuthal integrations within ±5° at horizontal (0°) and vertical (90°) regions of each SAXS pattern are conducted, they are denoted respectively as H- and V-integrations. Keeping in mind that the loading direction is "horizontal", the H and V regions of the SAXS pattern provide information of a subgroup of specifically orientated crystalline lamellae or blocks. Considering the PE-B quenched material as an example, the integrated *Lorentz-corrected* intensities (Iq^2) are plotted in **Figure 7** as a function of the norm of the scattering vector q.

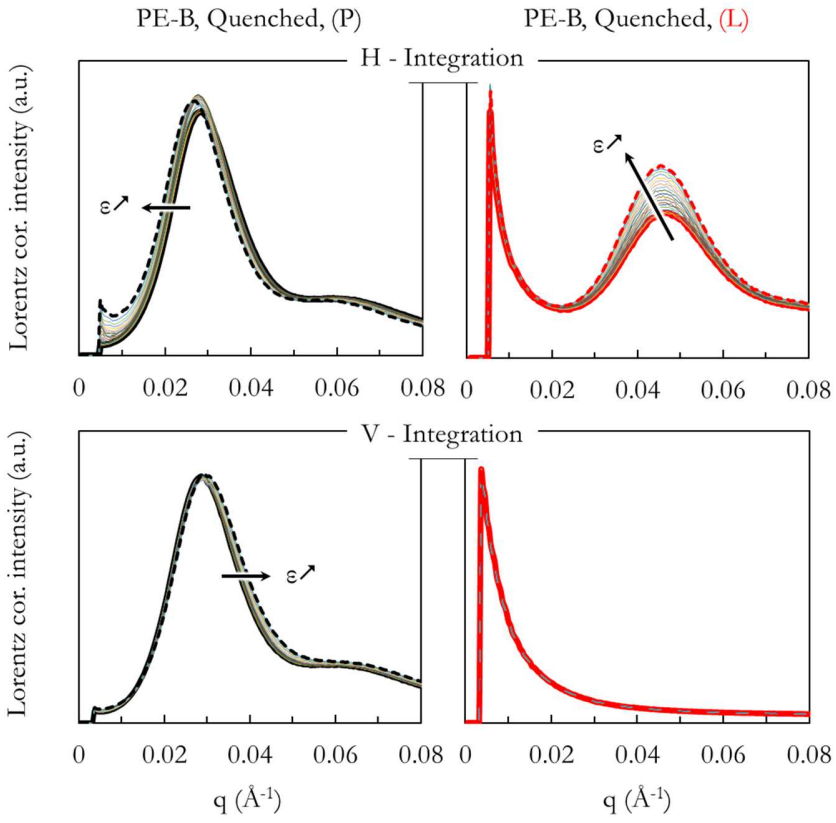

Figure 7: Lorentz-corrected intensities (Iq2) as a function of the norm of the scattering vector q in horizontal (H) and vertical (V) regions of the SAXS pattern for the Pristine (P) and L- necked (L) samples of the PE-B quenched material.

The q-position of a scattering peak (q_{max}) allows calculating the long period with **equation (2).**

$$L_P = \frac{2\pi}{q_{max}} \quad (2)$$

For pristine materials (**Figure 7** left), spherulitic structure consists of randomly oriented lamellae so that the profiles are identical by H- and V- integrations prior to deformation. Under uniaxial elongation, the q_{max} values of the scattering peaks in the horizontal zone 0° and vertical zone 90° tend to be lower and higher respectively: the equatorial lamellae (corresponding to horizontal SAXS zone) are subjected to tensile force and separate from one another, whereas the polar lamellae (corresponding to the vertical SAXS zone) get closer due to the Poisson's effect[61].

Focusing on the profiles obtained for the L-necked PE-B quenched sample (right in **Figure 7**) in the undeformed state, a scattering peak can only be observed by H-integration due to the orientation of the fibrils. At this stage, the long periods of the microfibrils (L_p^f) are listed in **Table 2** to compare with the long periods of pristine spherulitic structures (L_p^{sp}). For PE-A isothermal sample, L_p^f cannot be measured as the strong cavitation prohibits the observation of the scattering peak of lamellae. In other materials, it is found that $L_p^f < L_p^{sp}$, and the smaller long period values in the L-necked samples than the pristine ones can be explained by the melting-recrystallization or destruction-reconstruction [43,44] during fibrillar transformation. In details, the initial crystalline lamellae are fragmented and thinned due to the destruction and/or local melting whereas the small new crystalline bocks are created due to the strain-induced orientation of chains. Furthermore, L_p^f is seen to have limited dependency on the thermal treatment.

Table 2. Long periods of pristine samples and L-necked samples

	PE-A Quenched	PE-A Isothermal	PE-B Quenched	PE-B Isothermal
L_p^{sp} (nm)	22	35	20	33
L_p^f (nm)	15	-	13	13

Upon elongation, with increasing strain, the q_{max} value slightly decreases in the horizontal zone of SAXS pattern of the L-necked samples, indicating the same mechanism as the equatorial lamellae in the pristine samples. Due to the constant orientation of the crystalline structure, the evolution of q_{max} in the horizontal region along the deformation can be translated as the relative L_p^{sp} and L_p^f variations in order to calculate the local strain in the spherulitic equatorial and intra-fibrillar regions (marked in **Figure 8**) respectively using **equation (3)**. It is worth noting that this calculation is only adapted in the elastic regime (ε<0.05 is taken in this work).

$$\varepsilon_{local}(t) = \frac{\triangle L_p(t)}{L_{p0}} = \frac{L_p(t) - L_{p0}}{L_{p0}} \quad (3)$$

As shown in **Figure 8,** the local/macro strain ratios in equatorial/polar regions of pristine spherulites are about 0.4 ~ 0.5 and -0.25 ~ -0.17 respectively in all samples.

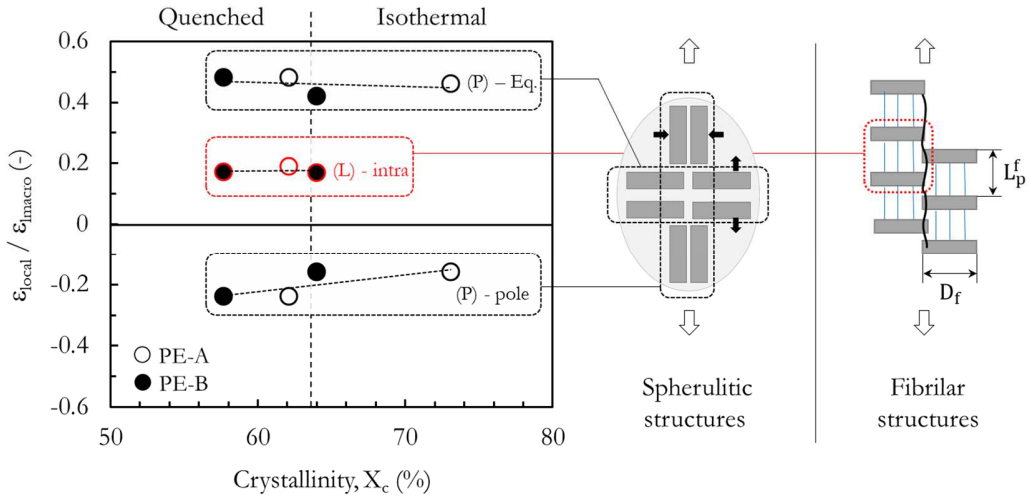

Figure 8: Local/macro strain ratios in Pristine (P) and L-necked (L) samples.

The low ratio (<1) at the equator is an evidence of the heterogeneous distribution of the stress triaxiality within the spherulitic structure[54,61]. The even lower local/macro strain ratio in the L-necked samples (about 0.17), suggests that the intra-fibrillar region should be more difficult to deform due to the stretched chains. The concept of the inter-fibrillar region is thus introduced. These chains are potentially more deformable than the intra-fibrillar ones along the pre-orientation. Thus, the macroscopic deformation of L-necked sample is mainly ascribed to the inter-fibrillar slide. The similar conclusion has been drawn in the work of Tang et al[62] for an over-stretched PE.

The measurement of the second microstructural parameter, the average width of micro-fibrils (D_f in **Figure 8** right) or crystalline blocks, is performed following a method proposed by Xiong et al.[43,44]. The scattering objects are assumed to be individually located in a medium of lower electron density without interference, D_f can thus be estimated by Guinier's law using a cylinder model (see **equation (4)**).

$$I(\mathrm{q}) = I_0 e^{\left(\frac{-q^2 R_g^2}{4}\right)} \tag{4}$$

Where R_g is the radius of gyration, the width of the crystalline blocks D_f=$2R_g$. In this case, the integration is performed at the center of the scattering patterns (where $qR_g \ll 1$). However, the cavity-induced scattering intensity is too strong so that it prevents this analysis in the V-region for certain L-necked samples and in the H-region for certain T-necked samples. However, thanks to the unidirectional character of the scattering factor of the highly oriented microfibrils, this analysis can be carried out in the H-region for L-necked samples and V-region for T-necked samples, where the scattering pattern is arisen from the periodic stacking of the crystal blocks[43]. The maximum deviation of D_f is 0.6 nm. It is worth noting that the variations of D_f during the tensile tests are all lower than the deviation value, indicating the stability of the crystalline width of micro-fibrils and suggesting that the fragmentation of lamellae can be neglected. In **Figure 9,** a correlation is found between the D_f and the stress transmitter density [ST] estimated by Brown's model: ST elements can generate the local stress concentration and induce the fragmentation of crystalline lamellae prior to the fibrillar transformation[43]. Therefore, with the higher ST concentration, the initial crystalline lamellae tend to be fragmented as the crystalline blocks with smaller width in the fibrillar state. Consequently, the tensile deformation of L-necked is mainly assigned to the inter-fibrillar slide, and no further fragmentation is observed.

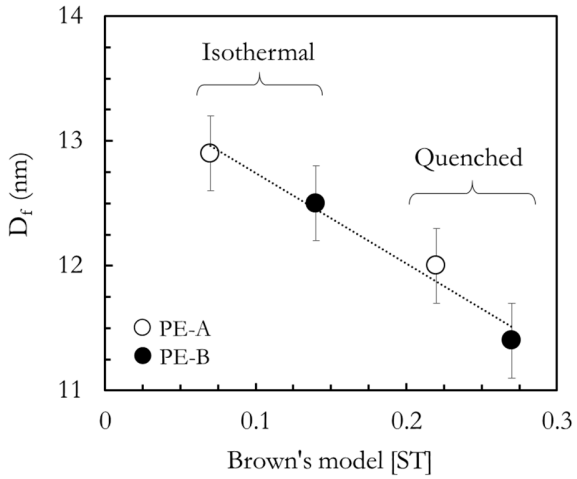

Figure 9: Correlation between the width of micro-fibrils D_f and initial [ST] value estimated by Brown's model. D_f does not change during the tensile loading.

T-necked samples:

For T-necked samples, the deformation behavior is quite different from the others: the gradual appearance and disappearance of scattering peaks can be observed respectively by H- and V-integrations with increasing strain (see **Figure 10a**). This evolution of pattern suggests a progressive 90° reorientation of crystalline blocks. The reorientation phase is finished approximately at the onset of the neck propagation (denoted as phase 1 in the mechanical profile, see **Figure 5**). **Figure 10b** displays the schematic of the reorientation of the crystalline blocks. Indeed, the inter-fibrillar chains not being confined should mainly contribute to the motion of crystalline blocks, and during this phase, the local deformation cannot be determined. Another possible interpretation to this reorientation phenomenon is that the microfibrils undergo another round of melting-recrystallization, the similar mechanism being described by Fu et al.[47]. Nevertheless, it is rather unlikely as the evolution of the pattern is continuous and it is thus difficult to imagine a continuous melting/crystallization process that lead to a continuous evolution of chain orientation without loss of the SAXS intensity scattering.

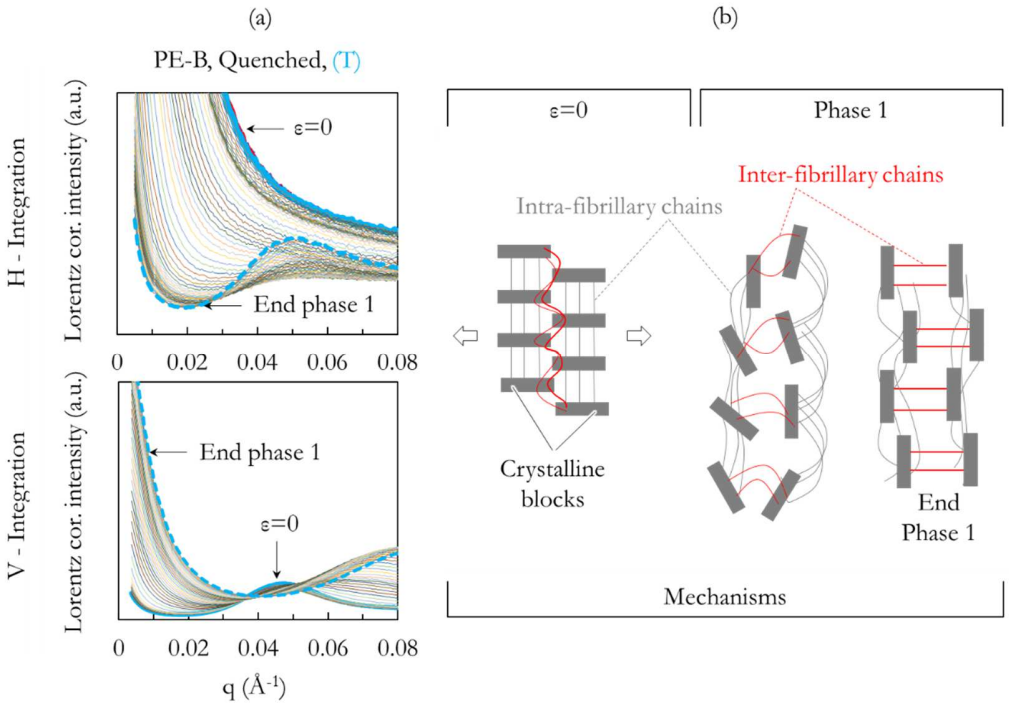

Figure 10: a) Lorentz-corrected intensities (Iq2) as a function of the norm of the scattering vector q at horizontal and vertical zones of the SAXS pattern for the T-necked PE-B quenched sample; b) Schematic of the reorientation of crystalline blocks during the tensile deformation of T-necked samples. Phase 1 is denoted in Figure 5.

However, during the neck propagation, which means that after the reorientation of the crystalline blocks, the configuration and dimension of the new fibrillar structure can be measured, as shown in **Table 3**, both the long period and width of crystalline blocks are stable before/after reorientation. The final dimensions of the microfibrils after the reorientation is identical to the initial one before rotation. According to these observations, it seems that the crystalline blocks only be rotated without measurable fragmentation during the necking initiation phase. Moreover, at the end of rotation, the same long period value suggests that the initial intra- and inter-fibrillar chains have the approaching ability of extension until being stretched.

Table 3. Long periods and average width of microfibrils before and after reorientation

	PE-A Quenched	PE-A Isothermal	PE-B Quenched	PE-B Isothermal
Before rotation: L_p^{f1} (nm)	15	-	13	13
After rotation: L_p^{f2} (nm)	14	-	13	13
Before rotation: D_f^{intra} (nm)	12	13	11	12
After rotation: D_f^2 (nm)	12	13	11	13

Failure stress of pristine, L-necked and T-necked samples

In the vicinity of fracture/failure point, the neck propagation is completed within the entire constant gauge of the sample so that the axial sample deformation is assumed to be homogenous. The specimens having the same initial geometry (value of thickness aside), so the difference in the ultimate failure stress between the pristine and necked samples are only related to the microstructural differences.

Figure 11a gathers the net failure stress of the pristine and necked samples of the four materials under study as a function of the initial crystallinity. The black, red and blue symbols correspond to the pristine, L-necked, and T-necked samples respectively. Due to the appearance of the cavities, especially in the isothermal samples, the final section of each specimen should be measured after the fracture in the nearby region (the measurements were made in regular regions about 0.5 mm from the fracture surface), the traditional isochoric assumption is not adapted. Despite uncertainties (see the error bar in **Figure 11a**), several important observations are valuable to be discussed. First, the failure stresses of the pristine and L-necked samples are similar, it means that, except the first loading, the influence of the consecutive cycles on the failure stress is neglected. Moreover, for a given material, these values are mainly related to the material type (or molecular structure), the PE-A samples exhibit higher values. The thermal treatments show limited influence.

Variation of the failure stress between the pristine (or L-necked) and T-necked samples is also evaluated in each material. Only in the PE-A isothermal samples having the highest crystallinity

and the lowest ST density, about 34% decrease of the failure stress is observed, indicating a significantly anisotropic failure stress of this material at fibrillar state. However, this anisotropy in other pre-necked materials are limited.

The following interpretation can be attempted:

Just before the failure, the stress is transmitted by the stretched STs: in the pristine and L-necked samples, the active stress transmitters are mainly in the intra-fibrillar region, whereas in the T-necked samples, the active stress transmitters are those in the initial inter-fibrillar region.

For a given material, it has been found that the final dimensions of the microfibrils (D_f and L_p^f) are similar in all the pristine and necked samples (no matter along which direction) thanks to *in-situ* SAXS characterization. Therefore, the different failure stresses should be related to the difference in the density/number of the active STs.

Regarding the PE-A isothermal material, the STs in the inter-fibrillar region should be much fewer than the intra-fibrillar STs. Indeed, for the PE who strongly cavitates (what we observed by SAXS and DIC), the voids are believed to be highly localized between the fibrillar structure, the assembly of the cavities and microfibrils is recognized as the craze[23] (see **Figure 11b**). The formation of craze is consistent with the heterogenous ST distribution in the intra- and inter-fibrillar regions: indeed, fewer STs exist in the inter-fibrillar region. The stretched chains bridging the edges of the craze can resist the growth of cavities when the sample is continuously deformed along the longitudinal direction, however, it should be easier to propagate these cavities along the transversal direction so that the failure stress is deteriorated. The cavitation is not a direct evidence for the damage but it can prove that the amorphous phase is not stable thus related to the low density of STs.

Especially, for other samples with higher initial ST density (including the PE-B isothermal sample), after the cyclic pre-loading induced fibrillation, the cavitation is relatively limited and ST distributions are thus almost homogenous in the intra- and inter- fibrillar regions (in accordance with the low cavity volume). Thus, the variation of stress and the anisotropy are both not obvious.

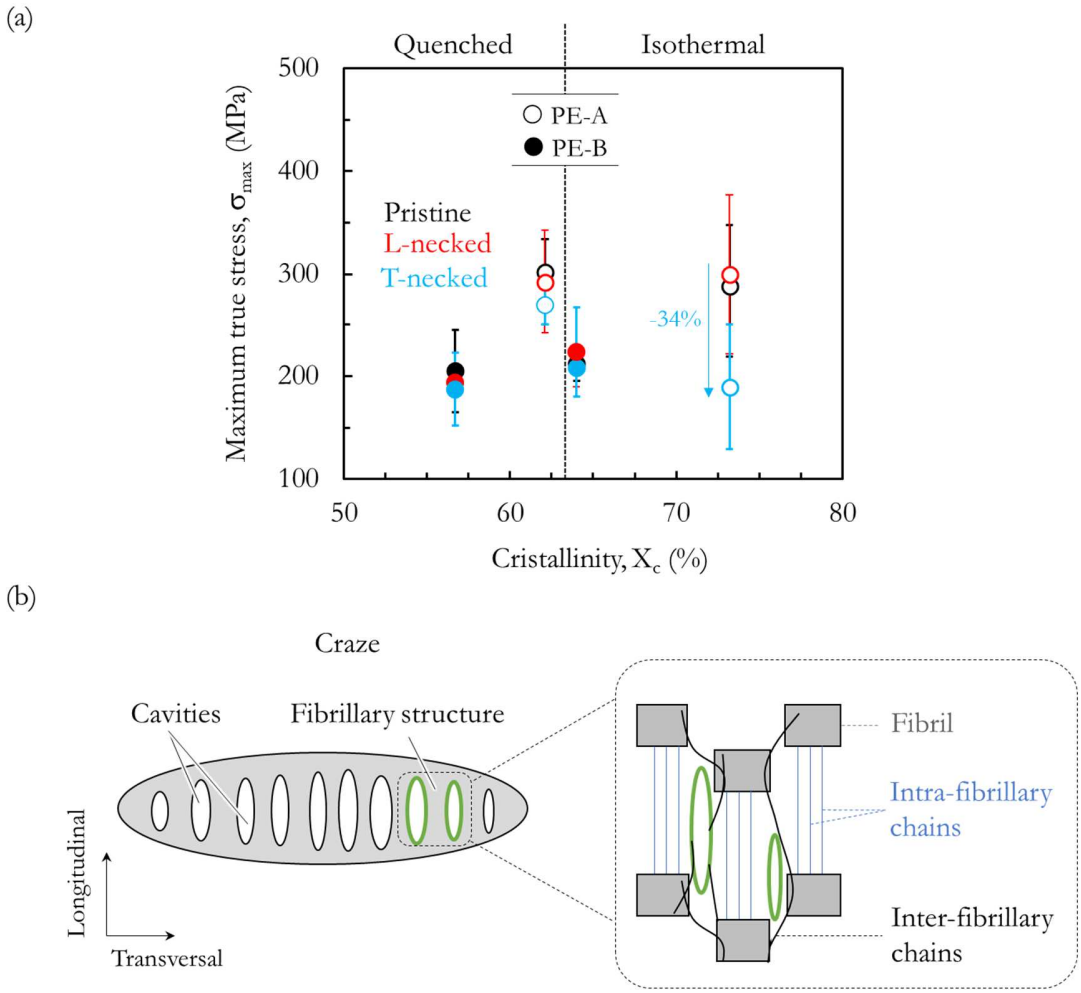

Figure 11: a) Failure stress in different samples; b) schematic of craze and the heterogeneous ST distribution in the intra- and inter-fibrillar regions in PE-A isothermal sample who strongly cavitates.

Conclusion

Being an important failure mode in semi-crystalline polymers, the evolution of necking during the mixed-mode oligo-cyclic deformation, the post-cyclic deformation and failure behaviors in the pre-necked HDPEs with different initial microstructures were investigated. During the consecutive cycles, the strain accumulation is continually localized along the longitudinal direction in the necked region, while the lateral width remains almost constant. The width reduction is highly related to the microstructure, it is more important in those quenched samples with higher content of amorphous phase (STs) and lower crystal dimensions. Clearly, the

significant reduction of width is also responsible for preventing the increase of volume due to the voids. The larger crystals should limit the lateral reduction due to Poisson's effect in amorphous phase, so that it is easier to generate the voids in those isothermal samples.

The deformation behavior of the necked HDPE samples is strongly anisotropic. Along the pre-loading orientation, stress transmitters in the intra-fibrillar region are already pre-stretched. The deformation mode is mainly related to the inter-fibrillar slide. An important contribution of this work is the study on the transversal deformation behavior. According to the in-situ SAXS measurements, all the crystalline blocks are rotated by inter-fibrillar STs. The melting-recrystallization may be not appropriate for the explanation, because the rotation of SAXS patterns is successive and continuous.

Along both the orthogonal directions, the final microstructural dimensions (long period and average width of microfibrils) remain identical. The true failure stress is thus associated with the different ST distribution (especially the tie chains) in the intra- and inter- fibrillar regions. Only in the PE-A isothermal samples, the STs in the inter-fibrillar region are fewer than in the intra-fibrillar region, this result is in accordance with the assumption that amounts of oriented cavities are located between the microfibrils, which should be easier to propagate while being subjected to a transverse loading.

In the industrial application, although PE-A samples show stronger initial failure stress, the one of isothermal sample is significantly deteriorated (in particular, along the transverse direction) after the oligo-cyclic tests. However, the PE-B samples conceived for pipeline application (PE-100), show relatively better stability during the oligo-cyclic deformation in both quenched and isothermal samples. These results are helpful to confirm the good oligo-cyclic performance of PE-B (commercial PE-100) materials, even under extreme crystallizing (isothermal) and cyclic (large strain) loading conditions, the most deformed part of the sample (necking) is still competent regarding the stress criterion.

Acknowledgments

The authors thank French SOLEIL synchrotron for the time assignation of SAXS/WAXS characterizations, Mr. PEREZ Javier for his help to install the *in-situ* experimental setup, training for post-process, INEOS (Brussels, Belgium) for supplying the PE pellets, EDF Research &

Development and EDF DIPNN Design and Technology branch for the grant of a doctoral fellowship to H. GUO.

Reference

[1] Hideki Omuro, Tomokazu Himono, POLYETHYLENE PIPELINE PERFORMANCE AGAINST EARTHQUAKE, in: 2018.
[2] Angelo Masi, Giuseppe Santarsiero, Domenico Nigro, Cyclic tests on external RC beam-column joints: role of seismic design level and axial load value on the ultimate capacity, Journal of Earthquake Engineering. 17 (2013) 110–136.
[3] Paolino Cassese, Paolo Ricci, Gerardo M. Verderame, Experimental study on the seismic performance of existing reinforced concrete bridge piers with hollow rectangular section, Engineering Structures. 144 (2017) 88–106.
[4] N. Nishonov, D. Bekmirzaev, E. An, Z. Urazmukhamedova, K. Turajonov, Behaviour and Calculation of Polymer Pipelines Under Real Earthquake Records, in: IOP Conference Series: Materials Science and Engineering, IOP Publishing, 2020: p. 052076.
[5] G. Ayoub, F. Zaïri, M. Naït-Abdelaziz, J.M. Gloaguen, Modeling the low-cycle fatigue behavior of visco-hyperelastic elastomeric materials using a new network alteration theory: application to styrene-butadiene rubber, Journal of the Mechanics and Physics of Solids. 59 (2011) 473–495.
[6] A.D. Drozdov, Cyclic viscoelastoplasticity and low-cycle fatigue of polymer composites, International Journal of Solids and Structures. 48 (2011) 2026–2040.
[7] Georges Ayoub, Fahmi Zaïri, Moussa Naït-Abdelaziz, Jean Michel Gloaguen, Modeling the low-cycle fatigue behavior of visco-hyperelastic elastomeric materials using a new network alteration theory: application to styrene-butadiene rubber, Journal of the Mechanics and Physics of Solids. 59 (2011) 473–495.
[8] J. Shi, A. Hu, F. Yu, Y. Cui, R. Yang, J. Zheng, Finite element analysis of high-density polyethylene pipe in pipe gallery of nuclear power plants, Nuclear Engineering and Technology. (2020).
[9] F. Detrez, S. Cantournet, R. Seguela, Plasticity/damage coupling in semi-crystalline polymers prior to yielding: Micromechanisms and damage law identification, Polymer. 52 (2011) 1998–2008.
[10] B. Klimkeit, S. Castagnet, Y. Nadot, A. El Habib, G. Benoit, S. Bergamo, C. Dumas, S. Achard, Fatigue damage mechanisms in short fiber reinforced PBT+ PET GF30, Materials Science and Engineering: A. 528 (2011) 1577–1588.
[11] H.-A. Cayzac, K. Saï, L. Laiarinandrasana, Damage based constitutive relationships in semi-crystalline polymer by using multi-mechanisms model, International Journal of Plasticity. 51 (2013) 47–64.
[12] I. Raphael, N. Saintier, G. Robert, J. Béga, L. Laiarinandrasana, On the role of the spherulitic microstructure in fatigue damage of pure polymer and glass-fiber reinforced semi-crystalline polyamide 6.6, International Journal of Fatigue. 126 (2019) 44–54.
[13] Y. Zhang, P.-Y.B. Jar, S. Xue, L. Li, Quantification of strain-induced damage in semi-crystalline polymers: a review, Journal of Materials Science. 54 (2019) 62–82.

[14] M. Elmeguenni, M. Naït-Abdelaziz, F. Zaïri, J.-M. Gloaguen, Fracture characterization of high-density polyethylene pipe materials using the $$$$-integral and the essential work of fracture, International Journal of Fracture. 183 (2013) 119–133.
[15] Y. Zhou, N. Brown, Anomalous fracture behaviour in polyethylenes under fatigue and constant load, Journal of Materials Science. 30 (1995) 6065–6069.
[16] L. Farge, J. Boisse, I. Bihannic, A. Diaz, S. André, Anisotropy development during HDPE necking studied at the microscale with in situ continuous 1D SAXS scans, Journal of Polymer Science Part B: Polymer Physics. 56 (2018) 170–181.
[17] R. Séguéla, On the Natural Draw Ratio of Semi-Crystalline Polymers: Review of the Mechanical, Physical and Molecular Aspects, Macromolecular Materials and Engineering. 292 (2007) 235–244.
[18] S. Humbert, O. Lame, G. Vigier, Polyethylene yielding behaviour: What is behind the correlation between yield stress and crystallinity?, Polymer. 50 (2009) 3755–3761.
[19] J. Ye, S. André, L. Farge, Kinematic study of necking in a semi-crystalline polymer through 3D Digital Image Correlation, International Journal of Solids and Structures. 59 (2015) 58–72.
[20] Z. Qi, N. Hu, D. Zeng, X. Su, Failure of high density polyethylene under cyclic loading: Mechanism analysis and mode prediction, International Journal of Mechanical Sciences. 156 (2019) 46–58.
[21] L. Laiarinandrasana, N. Selles, O. Klinkova, T.F. Morgeneyer, H. Proudhon, L. Helfen, Structural versus microstructural evolution of semi-crystalline polymers during necking under tension: Influence of the skin-core effects, the relative humidity and the strain rate, Polymer Testing. 55 (2016) 297–309.
[22] B. Xiong, O. Lame, J. M. Chenal, C. Rochas, Roland Seguela, G. Vigier, In-situ SAXS study and modeling of the cavitation/crystal-shear competition in semi-crystalline polymers: Influence of temperature and microstructure in polyethylene, Polymer. 54 (2013) 5408–5418.
[23] Andrzej Pawlak, Andrzej Galeski, Cavitation during tensile drawing of annealed high density polyethylene, Polymer. 51 (2010) 5771–5779.
[24] A. Pawlak, A. Galeski, A. Rozanski, Cavitation during deformation of semicrystalline polymers, Progress in Polymer Science. 39 (2014) 921–958.
[25] Sandrine Humbert, O. Lame, J. M. Chenal, C. Rochas, G. Vigier, New insight on initiation of cavitation in semicrystalline polymers: in-situ SAXS measurements, Macromolecules. 43 (2010) 7212–7221.
[26] N. Selles, P. Cloetens, H. Proudhon, T.F. Morgeneyer, O. Klinkova, N. Saintier, L. Laiarinandrasana, Voiding mechanisms in deformed polyamide 6 observed at the nanometric scale, Macromolecules. 50 (2017) 4372–4383.
[27] T.F. Morgeneyer, H. Proudhon, P. Cloetens, W. Ludwig, Q. Roirand, L. Laiarinandrasana, E. Maire, Nanovoid morphology and distribution in deformed HDPE studied by magnified synchrotron radiation holotomography, Polymer. 55 (2014) 6439–6443.
[28] A. Mesbah, M. Elmeguenni, Z. Yan, F. Zaïri, N. Ding, J.-M. Gloaguen, How stress triaxiality affects cavitation damage in high-density polyethylene: Experiments and constitutive modeling, Polymer Testing. (2021) 107248.
[29] Bijin Xiong, Olivier Lame, Jean-Marc Chenal, Yongfeng Men, Roland Seguela, Gerard Vigier, Critical stress and thermal activation of crystal plasticity in polyethylene: Influence of crystal microstructure and chain topology, Polymer. 118 (2017) 192–200.

[30] Y. Men, Critical Strains Determine the Tensile Deformation Mechanism in Semicrystalline Polymers, ACS Publications, 2020.
[31] G. Capaccio, T.A. Crompton, I.M. Ward, Drawing behavior of linear polyethylene. II. Effect of draw temperature and molecular weight on draw ratio and modulus, Journal of Polymer Science: Polymer Physics Edition. 18 (1980) 301–309.
[32] G. Meinel, A. Peterlin, Plastic deformation of polyethylene II. Change of mechanical properties during drawing, Journal of Polymer Science Part A-2: Polymer Physics. 9 (1971) 67–83.
[33] H. GUO, R.G. RINALDI, S. TAYAKOUT, M. BROUDIN, O. LAME, The correlation between the mixed-mode oligo-cyclic loading induced mechanical and microstructure changes in HDPE, Polymer. (2021) 123706. https://doi.org/10.1016/j.polymer.2021.123706.
[34] A. Chrysochoos, H. Louche, An infrared image processing to analyse the calorific effects accompanying strain localisation, International Journal of Engineering Science. 38 (2000) 1759–1788.
[35] B. Guelorget, M. François, G. Montay, Strain localization band width evolution by electronic speckle pattern interferometry strain rate measurement, Scripta Materialia. 60 (2009) 647–650.
[36] X. Poulain, L.W. Kohlman, W. Binienda, G.D. Roberts, R.K. Goldberg, A.A. Benzerga, Determination of the intrinsic behavior of polymers using digital image correlation combined with video-monitored testing, International Journal of Solids and Structures. 50 (2013) 1869–1878.
[37] M. Uchida, N. Tada, Sequential evaluation of continuous deformation field of semi-crystalline polymers during tensile deformation accompanied by neck propagation, International Journal of Plasticity. 27 (2011) 2085–2102.
[38] M. Andersen, O.S. Hopperstad, A.H. Clausen, Volumetric strain measurement of polymeric materials subjected to uniaxial tension, Strain. 55 (2019) e12314.
[39] A. Peterlin, Molecular model of drawing polyethylene and polypropylene, Journal of Materials Science. 6 (1971) 490–508.
[40] Frédéric Addiego, Stanislav Patlazhan, Kui Wang, Stéphane André, Sigrid Bernstorff, David Ruch, Time-resolved small-angle X-ray scattering study of void fraction evolution in high-density polyethylene during stress unloading and strain recovery, Polymer International. 64 (2015) 1513–1521.
[41] Frédéric Addiego, Abdesselam Dahoun, Christian G'Sell, Jean-Marie Hiver, Olivier Godard, Effect of microstructure on crazing onset in polyethylene under tension, Polymer Engineering & Science. 49 (2009) 1198–1205.
[42] H.-H. Kausch, R. Gensler, C. Grein, C.J.G. Plummer, P. Scaramuzzino, Crazing in semicrystalline thermoplastics, Journal of Macromolecular Science—Physics. 38 (1999) 803–815.
[43] S. Humbert, O. Lame, J.-M. Chenal, R. Seguela, G. Vigier, Memory effect of the molecular topology of lamellar polyethylene on the strain-induced fibrillar structure, European Polymer Journal. 48 (2012) 1093–1100.
[44] B. Xiong, O. Lame, J. M. Chenal, C. Rochas, Roland Seguela, On the strain-induced fibrillar microstructure of polyethylene: Influence of chemical structure, initial morphology and draw temperature, Express Polymer Letters. 10 (2016) 311.

[45] Z. Jiang, Y. Tang, J. Rieger, H.-F. Enderle, D. Lilge, S.V. Roth, R. Gehrke, W. Heckmann, Y. Men, Two lamellar to fibrillar transitions in the tensile deformation of high-density polyethylene, Macromolecules. 43 (2010) 4727–4732.
[46] T. Deplancke, M. Fivel, O. Lame, 1D strain rate-dependent constitutive model of UHMWPE: From crystalline network to fibrillar structure behavior, Mechanics of Materials. 137 (2019) 103129.
[47] L. Fu, Z. Jiang, H.-F. Enderle, D. Lilge, Z. Wu, S.S. Funari, Y. Men, Stretching temperature and direction dependency of uniaxial deformation mechanism in overstretched polyethylene, Journal of Polymer Science Part B: Polymer Physics. 52 (2014) 716–726. https://doi.org/10.1002/polb.23474.
[48] R.P. Janssen, D. de Kanter, L.E. Govaert, H.E. Meijer, Fatigue life predictions for glassy polymers: a constitutive approach, Macromolecules. 41 (2008) 2520–2530.
[49] Roel PM Janssen, Leon E. Govaert, Han EH Meijer, An analytical method to predict fatigue life of thermoplastics in uniaxial loading: sensitivity to wave type, frequency, and stress amplitude, Macromolecules. 41 (2008) 2531–2540.
[50] S. Lampman, B. Bonnie Sanders, N. Hrivnak, J. Kinson, C. Polakowski, Characterization and failure analysis of plastics: ASM International, Materials Park, OH, USA. (2003).
[51] B. Xiong, O. Lame, J.-M. Chenal, C. Rochas, R. Seguela, G. Vigier, Temperature-microstructure mapping of the initiation of the plastic deformation processes in polyethylene via in situ WAXS and SAXS, Macromolecules. 48 (2015) 5267–5275.
[52] A. Pawlak, A. Galeski, Plastic deformation of crystalline polymers: the role of cavitation and crystal plasticity, Macromolecules. 38 (2005) 9688–9697.
[53] F. Zaïri, M. Naït-Abdelaziz, J.-M. Gloaguen, J.-M. Lefebvre, A physically-based constitutive model for anisotropic damage in rubber-toughened glassy polymers during finite deformation, International Journal of Plasticity. 27 (2011) 25–51.
[54] H. Guo, R.G. Rinaldi, S. Tayakout, M. Broudin, O. Lame, Characterization of the spherulitic deformation in equatorial region and cavitation in HDPE materials submitted to mixed-mode oligo-cyclic tensile loading, Polymer Testing. 99 (2021) 107208. https://doi.org/10.1016/j.polymertesting.2021.107208.
[55] J.D. Hoffman, R.L. Miller, Kinetic of crystallization from the melt and chain folding in polyethylene fractions revisited: theory and experiment, Polymer. 38 (1997) 3151–3212.
[56] Y.-L. Huang, N. Brown, The effect of molecular weight on slow crack growth in linear polyethylene homopolymers, Journal of Materials Science. 23 (1988) 3648–3655.
[57] Y.-L. Huang, N. Brown, Dependence of slow crack growth in polyethylene on butyl branch density: morphology and theory, Journal of Polymer Science Part B: Polymer Physics. 29 (1991) 129–137.
[58] B. Xiong, Contribution to the study of elastic and plastic deformation mechanisms of polyethylene and polypropylene as a function of microstructure and temperature, Lyon, INSA, 2014.
[59] L. Laiarinandrasana, N. Selles, O. Klinkova, T.F. Morgeneyer, H. Proudhon, L. Helfen, Structural versus microstructural evolution of semi-crystalline polymers during necking under tension: Influence of the skin-core effects, the relative humidity and the strain rate, Polymer Testing. 55 (2016) 297–309.
[60] L. Laiarinandrasana, O. Klinkova, F. Nguyen, H. Proudhon, T.F. Morgeneyer, W. Ludwig, Three dimensional quantification of anisotropic void evolution in deformed semi-crystalline polyamide 6, International Journal of Plasticity. 83 (2016) 19–36.

[61] Bijin Xiong, Olivier Lame, Jean-Marc Chenal, Cyrille Rochas, Roland Seguela, Gerard Vigier, In-situ SAXS study of the mesoscale deformation of polyethylene in the pre-yield strain domain: Influence of microstructure and temperature, Polymer. 55 (2014) 1223–1227.
[62] Y. Tang, Z. Jiang, Y. Men, L. An, H.-F. Enderle, D. Lilge, S.V. Roth, R. Gehrke, J. Rieger, Uniaxial deformation of overstretched polyethylene: In-situ synchrotron small angle X-ray scattering study, Polymer. 48 (2007) 5125–5132.

Graphic abstract